

Dynamical analysis and localized waves of the *n*-component nonlinear Schrödinger equation with higher-order effects

Yu Lou(娄瑜) and Guoan Xu(许国安)

Citation: Chin. Phys. B, 2025, 34 (**3**): 030201. DOI: 10.1088/1674-1056/ada435
Journal homepage: http://cpb.iphy.ac.cn; http://iopscience.iop.org/cpb

What follows is a list of articles you may be interested in

Interaction solutions and localized waves to the (2+1)-dimensional Hirota-Satsuma-Ito equation with variable coefficient

Xinying Yan(闫鑫颖), Jinzhou Liu(刘锦洲), and Xiangpeng Xin(辛祥鹏)
Chin. Phys. B, 2023, 32 (**7**): 070201. DOI: 10.1088/1674-1056/acb9f2

Rational solutions and interaction solutions for (2 + 1)-dimensional nonlocal Schrödinger equation

Mi Chen(陈觅) and Zhen Wang(王振)
Chin. Phys. B, 2020, 29 (**12**): 120201. DOI: 10.1088/1674-1056/abc165

ocalized waves of the coupled cubic-quintic nonlinear Schrödinger equations in nonlinear optics

Tao Xu(徐涛), Yong Chen(陈勇), Ji Lin(林机)
Chin. Phys. B, 2017, 26 (**12**): 120201. DOI: 10.1088/1674-1056/26/12/120201

Localized waves of the coupled cubic-quintic nonlinear Schrödinger equations in nonlinear optics

Tao Xu(徐涛), Yong Chen(陈勇), Ji Lin(林机)
Chin. Phys. B, 2017, 26 (**12**): 120201. DOI: 10.1088/1674-1056/26/12/120201

Localized waves in three-component coupled nonlinear Schrödinger equation

Tao Xu(徐涛), Yong Chen(陈勇)
Chin. Phys. B, 2016, 25 (**9**): 090201. DOI: 10.1088/1674-1056/25/9/090201

Dynamical analysis and localized waves of the n-component nonlinear Schrödinger equation with higher-order effects

Yu Lou(娄瑜)[1,†] and Guoan Xu(许国安)[2]

[1] *Public Basic Education Department, Zhejiang Industry Polytechnic College, Shaoxing* 312000, *China*
[2] *School of Mathematical Science, Huaqiao University, Quanzhou* 362021, *China*

(Received 26 October 2024; revised manuscript received 4 December 2024; accepted manuscript online 31 December 2024)

Under investigation is the n-component nonlinear Schrödinger equation with higher-order effects, which describes the ultrashort pulses in the birefringent fiber. Based on the Lax pair, the eigenfunction and generalized Darboux transformation are derived. Next, we construct several novel higher-order localized waves and classified them into three categories: (i) higher-order rogue waves interacting with bright/antidark breathers, (ii) higher-order breather fission/fusion, (iii) higher-order breather interacting with soliton. Moreover, we explore the effects of parameters on the structure, collision process and energy distribution of localized waves and these characteristics are significantly different from previous ones. Finally, the dynamical properties of these solutions are discussed in detail.

Keywords: n-component nonlinear Schrödinger equation with higher-order effects, generalized Darboux transformation, localized waves, soliton, breather, rogue wave

PACS: 02.30.Ik, 02.30.Jr, 05.45.Yv

DOI: 10.1088/1674-1056/ada435 **CSTR:** 32038.14.CPB.ada435

1. Introduction

Recently, the field of localized waves has been the area of extremely animate research in mathematical physics and nonlinear science. Soliton, a well-known localized wave, has displayed the capability of propagating waves without losing the shape for a long distance.[1–3] Accordingly, soliton has attracted much research interest.[4–11] Breathers propagate steadily and are localized in either time or space, namely, Akhmediev breather (AB) and the Kuznetsov–Ma (KM) soliton.[12–17] The AB is developed from a weak periodic modulation, which is localized in the longitudinal dimension as it undergoes growth and decay. By contrast, the KM soliton undergoes periodic evolution with propagation. Rogue wave, an outlandish doubly localized wave packet, features a peaked hump three times the plane wave height and two side holes that appear as a result of energy conservation. Moreover, due to breathers' localized properties, rogue wave can be seen as the limiting case of AB and KM.[18,19] Breather and rogue wave are also widely investigated in many fields, such as nonlinear optics, oceanography, hydrodynamics, magnetics, plasma physics and so on.[20–26] In fact, it should be emphasized that interactions between localized waves lead to more rich novel wave structures and dynamic behaviors.[28–33]

As far as we know, due to the nonlinear superposition effect, interactions between localized waves may arouse waves with higher energy. To deeply understand the properties of localized waves in distinct fields, several approaches (e.g. the Bell polynomial,[34,35] KP hierarchy reduction method[36–38] and Darboux transformation (DT)[39–44]) are applied to explore localized waves of various nonlinear physical models. Among these models, one of the most concerned models is the nonlinear Schrödinger (NLS) equation which can explain many nonlinear phenomena and experimental results in erbium-doped fibre,[45] plasma,[46] and atmosphere.[47] Owing to the mutual influence of relative velocities between diverse component fields and the common coupling effect of cross-phase modulation, multi-component nonlinear models can derive more profuse physical phenomena than single-component models.[48–51] Besides, another notable characteristic is that multi-component models can abstract and show complicated physical wave propagations by means of concise mathematical formulas. Therefore, it is worthwhile to examine the n-component NLS equations

$$\mathrm{i}\boldsymbol{u}_t+\frac{1}{2}\boldsymbol{u}_{xx}+\boldsymbol{u}\boldsymbol{u}^{\dagger}\boldsymbol{u}=0, \tag{1}$$

where $\boldsymbol{u}=(u_1,u_2,\ldots,u_n)^{\mathrm{T}}$, $u_j(x,t)$ $(j=1,2,\ldots,n)$ are complex functions and '†' denotes the Hermite conjugation.

Nevertheless, it can be seen that the NLS equation cannot explain the propagation of soliton-type pulses in the femtosecond range. For high-intensity ultrashort pulses in the femtosecond range, it is necessary to incorporate the higher-order effect such as the third-order dispersion (TOD), self-steepening (SS) and stimulated Raman scattering (SRS).[52–57] The effect of TOD is a splitting of higher-order solitons. SS gives the plus a very narrow width in the course of the propagation because the peak of the pulse will travel slower than the

†Corresponding author. E-mail: lyzjipc@163.com

© 2025 Chinese Physical Society and IOP Publishing Ltd. All rights, including for text and data mining, AI training, and similar technologies, are reserved.

wings. The self-frequency shift is a self-induced redshift in the pulse spectrum arising from SRS. The long wavelength components of the pulse experience Raman gain at the express of the short wavelength components, leading to a increasing redshift as the pulse propagates. Considering the impact of the coupling terms and higher-order effects, one mainly studies the n-component nonlinear Schrödinger equation with higher-order effects

$$\begin{aligned}&\mathrm{i}\boldsymbol{u}_t+\frac{1}{2}\boldsymbol{u}_{xx}+\boldsymbol{u}\boldsymbol{u}^{\dagger}\boldsymbol{u}\\&+\gamma\bigg(\frac{1}{2}\boldsymbol{u}_{xxxx}+\boldsymbol{u}(\boldsymbol{u}_x^{\dagger}\boldsymbol{u})_x+\boldsymbol{u}_x\boldsymbol{u}_x^{\dagger}\boldsymbol{u}+2(\boldsymbol{u}_{xx}\boldsymbol{u}^{\dagger}\boldsymbol{u}+\boldsymbol{u}\boldsymbol{u}^{\dagger}\boldsymbol{u}_{xx})\\&+3(\boldsymbol{u}_x\boldsymbol{u}^{\dagger}\boldsymbol{u}_x+\boldsymbol{u}(\boldsymbol{u}^{\dagger}\boldsymbol{u})^2)\bigg)=0,\end{aligned}\tag{2}$$

where γ is a real parameter which measures the strength of higher-order linear and nonlinear effects. As we know, there have been various works on Eq. (2).[58–64] Therefore, one pays attention to succeed it and gets some novel localized waves, which can be classified into three categories: (i) higher-order rogue waves interacting with bright/antidark breathers, (ii) higher-order breather fission/fusion, (iii) higher-order breather interacting with soliton. To our knowledge, there is no report of these three kinds of localized waves of any n-component nonlinear Schrödinger equation with higher-order effects.

The outline of the study is organized. In Section 2, based on the Lax pair, the eigenfunction and generalized DT of Eq. (2) are constructed. In Section 3, by using the generalized DT, we get three types of novel localized waves for Eq. (2). Then we take 2-component and 3-component as examples and perform the dynamical analysis of these solutions. The conclusion is given in Section 5.

2. Generalized Darboux transformation

The Lax pair of Eq. (2) is

$$\begin{aligned}&\boldsymbol{\Phi}_x=U\boldsymbol{\Phi},\quad U=\mathrm{i}\lambda\sigma+\mathrm{i}P,\\&\boldsymbol{\Phi}_t=V\boldsymbol{\Phi},\quad V=\sum_{j=0}^{4}\lambda^j V_j,\end{aligned}\tag{3}$$

with

$$\begin{aligned}P&=\begin{pmatrix}0&\boldsymbol{u}^{\dagger}\\\boldsymbol{u}&\boldsymbol{0}_{n\times n}\end{pmatrix},\quad \sigma=\begin{pmatrix}1&\boldsymbol{0}_{1\times n}\\\boldsymbol{0}_{n\times 1}&-I_n\end{pmatrix},\\V_4&=-4\mathrm{i}\gamma\sigma,\quad V_3=-4\mathrm{i}\gamma P,\\V_2&=2\gamma(\mathrm{i}P^2\sigma-\sigma P_x)+\mathrm{i}\sigma,\\V_1&=\gamma(\mathrm{i}P_{xx}+2\mathrm{i}P^3-PP_x+P_xP)+\mathrm{i}P,\\V_0&=\frac{\gamma}{2}[\sigma(P_{xxx}-\mathrm{i}PP_{xx}-\mathrm{i}P_{xx}P-3\mathrm{i}P^4+3P^2P_x\\&\quad+3P_xP^2)+\mathrm{i}P_x^2\sigma]+\frac{1}{2}\sigma(P_x-\mathrm{i}P^2),\end{aligned}$$

where I_n is a $n\times n$ identity matrix and λ is a spectral parameter. It is easy to see that the compatibility condition $U_t-V_x+[U,V]=0$ can lead to Eq. (2).

After that, one can construct the DT of Eq. (2) as follows:

$$D[1]=I_{n+1}-\frac{\lambda_1-\lambda_1^*}{\lambda-\lambda_1^*}\frac{\boldsymbol{\Phi}_0\boldsymbol{\Phi}_0^{\dagger}}{\boldsymbol{\Phi}_0^{\dagger}\boldsymbol{\Phi}_0},\tag{4}$$

where $\boldsymbol{\Phi}_0=(\phi_1,\phi_2,\ldots,\phi_n)^{\mathrm{T}}$ solves the Lax pair (3) with $\lambda=\lambda_1$. Then the new functions can be written as

$$u_j=u_j[0]+\frac{2\mathrm{i}(\lambda_1-\lambda_1^*)\phi_1^*\phi_{j+1}}{|\phi_1|^2+|\phi_2|^2+|\phi_3|^2},\quad j=1,2,\ldots,n.\tag{5}$$

Theorem 1 Let $\boldsymbol{\Phi}[\lambda_1(1+\varepsilon)]$ be a solution of Eq. (3) with $\lambda=\lambda_1(1+\varepsilon)$ and an initial solution $u_j[0]$ $(j=1,2,\ldots,n)$. If $\boldsymbol{\Phi}[\lambda_1(1+\varepsilon)]$ can be expanded at $\varepsilon=0$,

$$\boldsymbol{\Phi}[\lambda_1(1+\varepsilon)]=\boldsymbol{\Phi}_0+\boldsymbol{\Phi}_1\varepsilon+\boldsymbol{\Phi}_2\varepsilon^2+\cdots,\tag{6}$$

then

$$\begin{aligned}\boldsymbol{\Phi}[N]&=(\phi_1[N],\phi_2[N],\ldots,\phi_n[N])^{\mathrm{T}}\\&=\lambda_1\boldsymbol{\Phi}[N-1]+D[N-1]\Xi[N],\quad N=2,3,\ldots,\\\boldsymbol{\Phi}[0]&=(\phi_1[0],\phi_2[0],\ldots,\phi_n[0])^{\mathrm{T}}=\boldsymbol{\Phi}_0,\\\Xi[N]&=\boldsymbol{\Phi}[N](\boldsymbol{\Phi}_{j+1}\to\boldsymbol{\Phi}_{j+2}),\quad j=0,1,2,\ldots\end{aligned}\tag{7}$$

with

$$\begin{aligned}D[l]&=(\lambda-\lambda_1^*)I_{n+1}+(\lambda_1^*-\lambda_1)\frac{\boldsymbol{\Phi}[l-1]\boldsymbol{\Phi}[l-1]^{\dagger}}{\boldsymbol{\Phi}[l-1]^{\dagger}\boldsymbol{\Phi}[l-1]},\\&\quad l=1,2,\ldots,N-1\end{aligned}\tag{8}$$

are solutions of Eq. (3) with respect to the same spectral parameter λ_1.

Then the solutions $u_j[N]$ $(j=1,2,\ldots,n)$ read

$$\begin{aligned}u_j[N]&=u_j[N-1]\\&\quad+\frac{2\mathrm{i}(\lambda_1-\lambda_1^*)\phi_1^*[N-1]\phi_{j+1}[N-1]}{|\phi_1[N-1]|^2+|\phi_2[N-1]|^2+|\phi_3[N-1]|^2}.\end{aligned}\tag{9}$$

To present three different kinds of localized waves for Eq. (2), we take the following initial solutions:

$$\begin{aligned}&u_j[0]=a_j\mathrm{e}^{\mathrm{i}\theta t},\quad \theta=2\omega^2+6\gamma\omega^4,\\&\omega^2=\sum_{j=1}^{n}a_j^2,\quad j=1,2,\ldots,n,\end{aligned}\tag{10}$$

where a_j are real constants. Introducing a gauge transformation

$$\boldsymbol{\Phi}=A\boldsymbol{\Psi},\quad A=\mathrm{diag}(1,\mathrm{e}^{\mathrm{i}\theta t}I_n)\tag{11}$$

can generate

$$\boldsymbol{\Psi}_x=\widetilde{U}\boldsymbol{\Psi},\quad \boldsymbol{\Psi}_t=\widetilde{V}\boldsymbol{\Psi},\tag{12}$$

with

$$\widetilde{U}=\mathrm{i}\lambda\sigma+\widetilde{U}_0,$$

$$\widetilde{V} = \mathrm{i}(4\gamma\lambda^2-3\gamma\omega^2-1)\widetilde{U}^2+2\lambda(4\gamma\lambda^2-2\gamma\omega^2-1)\widetilde{U} +4\mathrm{i}\gamma\lambda^4+\mathrm{i}\gamma\lambda^2\omega^2-6\mathrm{i}\gamma\omega^4+\mathrm{i}\lambda^2-2\mathrm{i}\omega^2,$$

$$\widetilde{U}_0 = \begin{pmatrix} 0 & \boldsymbol{a} \\ \boldsymbol{a} & \mathbf{0}_{n\times n} \end{pmatrix}, \quad \boldsymbol{a} = (a_1, a_2, \ldots, a_n)^{\mathrm{T}}.$$

Hence, the solution for system (3) can be written as

$$\Phi = AFGZ, \tag{13}$$

where

$$F = \mathrm{e}^{\widetilde{U}x}, \quad G = \mathrm{e}^{\widetilde{V}t},$$

and Z is a free vector.

After complicated calculations, F can be written by

$$F = \frac{1}{\xi}\begin{pmatrix} \Gamma_0 & -\Gamma_1^{\mathrm{T}} \\ \Gamma_1 & \Gamma_2 \end{pmatrix}, \tag{14}$$

with

$$\Gamma_0 = \xi\cosh(\xi x)+\mathrm{i}\lambda\sinh(\xi x),$$
$$\Gamma_1 = [a_1\sinh(\xi x), a_2\sinh(\xi x), \ldots, a_n\sinh(\xi x)]^{\mathrm{T}},$$
$$\Gamma_2 = \begin{pmatrix} a_1^2\omega^{-2}\vartheta+(\omega-a_1^2)\xi\omega^{-2}\mathrm{e}^{-\mathrm{i}\lambda x} & a_1a_2\omega^{-2}\Lambda & \cdots & a_1a_n\omega^{-2}\Lambda \\ a_1a_2\omega^{-2}\Lambda & a_2^2\omega^{-2}\vartheta+(\omega-a_2^2)\xi\omega^{-2}\mathrm{e}^{-\mathrm{i}\lambda x} & \cdots & a_2a_n\omega^{-2}\Lambda \\ \vdots & \vdots & \ddots & \vdots \\ a_1a_n\omega^{-2}\Lambda & a_1a_n\omega^{-2}\Lambda & \cdots & a_n^2\omega^{-2}\vartheta+(\omega-a_n^2)\xi\omega^{-2}\mathrm{e}^{-\mathrm{i}\lambda x} \end{pmatrix},$$
$$\Lambda = \vartheta-\xi\mathrm{e}^{-\mathrm{i}\lambda x}, \quad \vartheta = \xi\cosh(\xi x)-\mathrm{i}\lambda\sinh(\xi x), \quad \xi = \mathrm{i}\sqrt{\lambda^2+\omega^2}.$$

In the same token, G can be expressed as

$$G = \frac{1}{\xi}\mathrm{e}^{-\frac{\mathrm{i}\theta t}{2}}\begin{pmatrix} \Xi_0 & -\Xi_1^{\mathrm{T}} \\ \Xi_1 & \Xi_2 \end{pmatrix}, \tag{15}$$

with

$$\Xi_0 = \xi\cosh(\eta t)+\mathrm{i}\lambda\sinh(\eta t),$$
$$\Xi_1 = [a_1\sinh(\eta t),\ a_2\sinh(\eta t),\ \ldots,\ a_n\sinh(\eta t)]^{\mathrm{T}},$$
$$\Xi_2 = \begin{pmatrix} a_1^2\omega^{-2}\rho+(\omega-a_1^2)\xi\omega^{-2}\mathrm{e}^{-\mathrm{i}\nu t} & a_1a_2\omega^{-2}\Omega & \cdots & a_1a_n\omega^{-2}\Omega \\ a_1a_2\omega^{-2}\Omega & a_2^2\omega^{-2}\rho+(\omega-a_2^2)\xi\omega^{-2}\mathrm{e}^{-\mathrm{i}\nu t} & \cdots & a_2a_n\omega^{-2}\Omega \\ \vdots & \vdots & \ddots & \vdots \\ a_1a_n\omega^{-2}\Omega & a_1a_n\omega^{-2}\Omega & \cdots & a_n^2\omega^{-2}\rho+(\omega-a_n^2)\xi\omega^{-2}\mathrm{e}^{-\mathrm{i}\nu t} \end{pmatrix},$$
$$\Omega = \rho-\xi\mathrm{e}^{-\mathrm{i}\nu t}, \quad \rho = \xi\cosh(\eta t)-\mathrm{i}\lambda\sinh(\eta t), \quad \eta = (4\gamma\lambda^3-(2\gamma\omega^2+1)\lambda)\xi, \quad \nu = 3\gamma\omega^4+\omega^2+2\lambda^2-8\gamma\lambda^4.$$

Theorem 2 Taking into account a Taylor series expansion in Eqs. (5) and (13), one gets the following formulas:

$$F|_{\lambda=\lambda_1(1+\varepsilon)} = \sum_{n=0}^{\infty}F_n\varepsilon^n, \quad G|_{\lambda=\lambda_1(1+\varepsilon)} = \mathrm{e}^{-\frac{\mathrm{i}\theta t}{2}}\sum_{n=0}^{\infty}G_n\varepsilon^n, \tag{16}$$

where F_n and G_n represent the nth coefficient matrix of ε. And Z reads

$$Z = \sum_{j=0}^{\infty}Z_j\varepsilon^j, \tag{17}$$

where Z_j are constant vectors. Consequently, we have

$$\Phi = \sum_{n=0}^{\infty}\Phi_n\varepsilon^n, \quad \Phi_n = \mathrm{e}^{-\frac{\mathrm{i}\theta t}{2}}A\sum_{k=0}^{n}\sum_{j=0}^{n}F_kG_jZ_{n-k-j}. \tag{18}$$

3. Dynamical analysis and localized waves of Eq. (2)

In this section, we will exhibit three kinds of higher-order localized waves. The structure, collision process and energy distribution of these solutions depend on the values of $a_1, a_2, \ldots, a_n$ and Z_j $(j = 0, 1, 2, \ldots)$. In order to make the results of this paper more meaningful, we will construct some novel localized waves which were never reported for Eq. (2). By examining (i) $\mathrm{Im}(\lambda_1) = \omega$, (ii) $-\omega < \mathrm{Im}(\lambda_1) < \omega$, (iii) $\mathrm{Im}(\lambda_1) > \omega$, we can divide the solutions into three kinds. Next, we will take the 2-component and 3-component Eq. (2) as examples to discuss the results of three cases respectively.

3.1. Dynamical analysis and localized waves of 2-component Eq. (2)

In view of Theorems 1 and 2, we can attain the first-order localized waves of 2-component Eq. (2) as follows:

$$u_1[1] = u_1[0]+2\mathrm{i}(\lambda_1-\lambda_1^*)\frac{\phi_1^*[0]\phi_2[0]}{|\phi_1[0]|^2+|\phi_2[0]|^2+|\phi_3[0]|^2}, \tag{19}$$

$$u_2[1] = u_2[0]+2\mathrm{i}(\lambda_1-\lambda_1^*)\frac{\phi_1^*[0]\phi_3[0]}{|\phi_1[0]|^2+|\phi_2[0]|^2+|\phi_3[0]|^2}, \tag{20}$$

with

$$(\phi_1[0],\phi_2[0],\phi_3[0])^{\mathrm{T}} = AF_0G_0Z_0. \tag{21}$$

Case A: $\mathrm{Im}(\lambda_1)=\omega$

For $N=1$, we take $\lambda_1=\mathrm{i}\omega$ which results in the following expressions:

$$F_0=\begin{pmatrix} 1-\omega x & -a_1x & -a_2x \\ a_1x & a_1^2\omega^{-2}f_0+\mathrm{e}^{\omega x} & a_1a_2\omega^{-2}f_0 \\ a_2x & a_1a_2\omega^{-2}f_0 & a_2^2\omega^{-2}f_0+\mathrm{e}^{\omega x}\end{pmatrix},\quad G_0=\begin{pmatrix} 1+\mathrm{i}\omega^2g_0t & \mathrm{i}a_1\omega g_0t & \mathrm{i}a_2\omega g_0t \\ -\mathrm{i}a_1\omega g_0t & a_1^2\omega^{-2}g_1+\mathrm{e}^{\mathrm{i}(5\mathrm{i}\gamma\omega^2)\omega^2t} & a_1a_2g_1 \\ -\mathrm{i}a_2\omega g_0t & a_1a_2g_1 & a_2^2\omega^{-2}g_1+\mathrm{e}^{\mathrm{i}(5\mathrm{i}\gamma\omega^2)\omega^2t}\end{pmatrix},$$

$$f_0=1+\omega x+\mathrm{e}^{\omega x},\quad g_0=1+6\gamma\omega^2,\quad g_1=1-6\mathrm{i}\gamma\omega^4t-\mathrm{i}\omega^2t-\mathrm{e}^{\mathrm{i}(5\mathrm{i}\gamma\omega^2)\omega^2t}.$$

It can be observed that the first-order localized wave consists of rogue wave and breather in Fig. 1. If $a_1=a_2=1$, the structures of the breathers in the u_1 and u_2 components are similar. If a_1 or a_2 is not equal to 1, the structures of breathers in Figs. 1(c) and 1(d) are extremely distinct. Figure 1(c) shows the antidark breather whose amplitudes on the plane are lower than the ones under the plane while Fig. 1(d) shows the opposite.

For $N=2$, one works out the second-order rogue waves interacting with two breathers in Figs. 2 and 3. It is remarkable that with the values of z_{11} and z_{31} increasing simultaneously, the second-order rogue wave in u_1 component moves along the negative direction of the x-axis from the origin of the coordinate, while the second-order wave in u_1 component travels toward the positive direction (see Figs. 2(c), 2(d), 3(c), and 3(d)). On the other hand, we find that increasing the values of z_{11} and z_{31} leads to the amplitude of the second-order rogue wave being small. The reason is that the energy producing the rogue wave is transformed into the kinetic energy that promotes the movement of the rogue wave. It can be seen that the energy of the process is conserved.

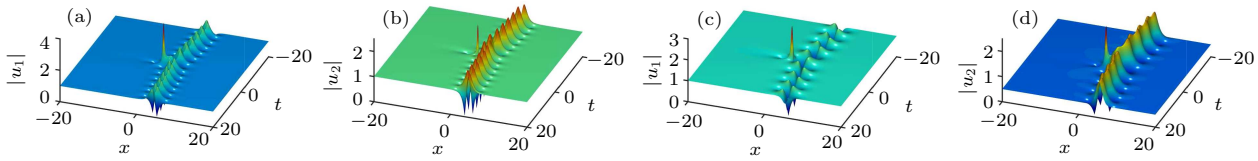


Fig. 1. The first-order rogue wave interacts with breather with (a), (b) $a_1=1$, $a_2=1$, $\gamma=1/10$, $z_{10}=1$, $z_{20}=2$, $z_{30}=3$; (c), (d) $a_1=1$, $a_2=1/2$, $\gamma=1/10$, $z_{10}=1$, $z_{20}=1$, $z_{30}=1$.

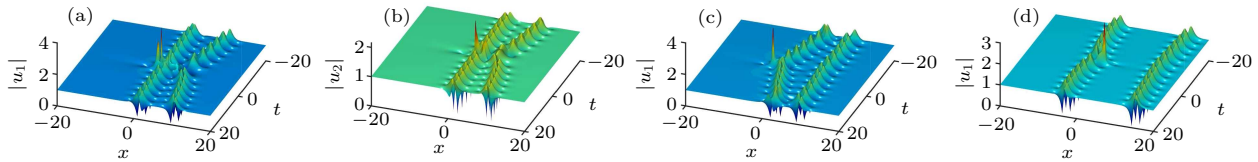


Fig. 2. The second-order rogue waves interact with breathers with $a_1=1$, $a_2=1$, $\gamma=1/10$, $z_{10}=1$, $z_{20}=2$, $z_{30}=1$, (a), (b) $z_{11}=1$, $z_{21}=0$, $z_{31}=1$; (c), (d) $z_{11}=1000$, $z_{21}=0$, $z_{31}=1000$.

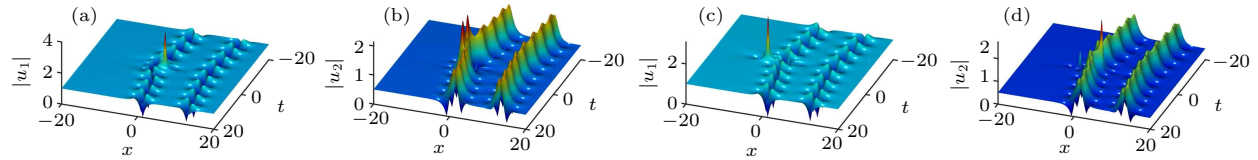


Fig. 3. The second-order rogue waves interact with breathers with $a_1=1$, $a_2=1/2$, $\gamma=1/10$, $z_{10}=1$, $z_{20}=1$, $z_{30}=1$, (a), (b) $z_{11}=1$, $z_{21}=0$, $z_{31}=1$; (c), (d) $z_{11}=1000$, $z_{21}=0$, $z_{31}=1000$.

Case B: $-\omega<\mathrm{Im}(\lambda_1)<\omega$

For $N=1$, by considering $-\omega<\mathrm{Im}(\lambda_1)<\omega$, the elements of matrices F_0 and G_0 can be obtained as

$$F_0=\begin{pmatrix} -\frac{\sqrt{3}}{3}f_0 & -\frac{2\sqrt{3}}{3}a_1\omega^{-1}\sin\left(\frac{\sqrt{3}}{2}x\right) & -\frac{2\sqrt{3}}{3}a_2\omega^{-1}\sin\left(\frac{\sqrt{3}}{2}x\right) \\ \frac{2\sqrt{3}}{3}a_1\omega^{-1}\sin\left(\frac{\sqrt{3}}{2}x\right) & \frac{\sqrt{3}}{3}a_1^2\omega^{-2}(f_1-\sqrt{3}\mathrm{e}^{\omega x})+\mathrm{e}^{\omega x} & \frac{\sqrt{3}}{3}a_1a_2\omega^{-2}(f_1-\sqrt{3}\mathrm{e}^{\omega x}) \\ \frac{2\sqrt{3}}{3}a_2\omega^{-1}\sin\left(\frac{\sqrt{3}}{2}x\right) & \frac{\sqrt{3}}{3}a_1a_2\omega^{-2}(f_1-\sqrt{3}\mathrm{e}^{\omega x}) & \frac{\sqrt{3}}{3}a_2^2\omega^{-2}(f_1-\sqrt{3}\mathrm{e}^{\omega x})+\mathrm{e}^{\omega x}\end{pmatrix},$$

$$G_0=\begin{pmatrix} \frac{\sqrt{3}}{3}g_0 & \frac{2\sqrt{3}}{3}\mathrm{i}a_1\omega^{-1}\sinh(\mu t) & \frac{2\sqrt{3}}{3}\mathrm{i}a_2\omega^{-1}\sinh(\mu t) \\ -\frac{2\sqrt{3}}{3}\mathrm{i}a_1\omega^{-1}\sinh(\mu t) & -\frac{\sqrt{3}}{3}\omega^{-2}(a_1^2g_1+\sqrt{3}(a_1^2-\omega^2)\mathrm{e}^{-\frac{\mathrm{i}(1+5\gamma\omega^2)\omega^2}{2}t}) & -\frac{\sqrt{3}}{3}\omega^{-2}a_1a_2(g_1+\mathrm{e}^{-\frac{\mathrm{i}(1+5\gamma\omega^2)\omega^2}{2}t}) \\ -\frac{2\sqrt{3}}{3}\mathrm{i}a_2\omega^{-1}\sinh(\mu t) & -\frac{\sqrt{3}}{3}\omega^{-2}a_1a_2(g_1+\mathrm{e}^{-\frac{\mathrm{i}(1+5\gamma\omega^2)\omega^2}{2}t}) & -\frac{\sqrt{3}}{3}\omega^{-2}(a_2^2g_1+\sqrt{3}(a_2^2-\omega^2)\mathrm{e}^{-\frac{\mathrm{i}(1+5\gamma\omega^2)\omega^2}{2}t}) \end{pmatrix},$$

$$f_0=\sqrt{3}\cos\left(\frac{\sqrt{3}}{2}x\right)-\sin\left(\frac{\sqrt{3}}{2}x\right),\quad f_1=\sqrt{3}\cos\left(\frac{\sqrt{3}}{2}x\right)+\sin\left(\frac{\sqrt{3}}{2}x\right),$$

$$g_0=\sqrt{3}\cosh(\mu t)+\mathrm{i}\sinh(\mu t),\quad g_1=-\sqrt{3}\cosh(\mu t)+\mathrm{i}\sinh(\mu t),\quad \mu=\frac{\sqrt{3}\omega^2(1+3\gamma\omega^2)}{4}.$$

We achieve the fission/fusion phenomenon of the breather in Figs. 4 and 5. It can be noticed that the breather propagates stably at the beginning, while it divides into two breathers at $x=0$ in Fig. 4. Moreover, after fission, the shape of the breather becomes larger and the amplitude becomes smaller. Because the energy producing one breather is divided into two parts which means the total energy of the fission process is conserved. The breather fusion is shown in Fig. 5. We can observe that two breathers converge to one antidark breather at $x=0$. Obviously, the total energy of the fusion process is also conserved. More importantly, it is apparent that different values of a_2 cause the structures of breather fission or fusion changing a lot. Comparing breather fission with breather fusion, we find that the fission phenomenon of breather presents the bright breather, while the fusion phenomenon of breather presents the antidark breather.

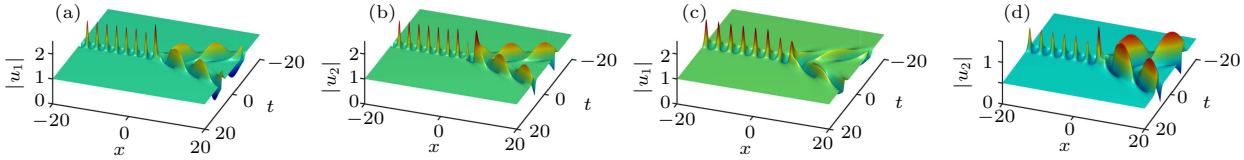


Fig. 4. The first-order breather fission with (a), (b) $a_1=1$, $a_2=1$, $\gamma=1/10$, $\lambda_1=\mathrm{i}\sqrt{2}/2$, $z_{10}=1$, $z_{20}=2$, $z_{30}=3$; (c), (d) $a_1=1$, $a_2=1/2$, $\gamma=1/10$, $\lambda_1=\mathrm{i}\sqrt{2}/2$, $z_{10}=1$, $z_{20}=1$, $z_{30}=1$.

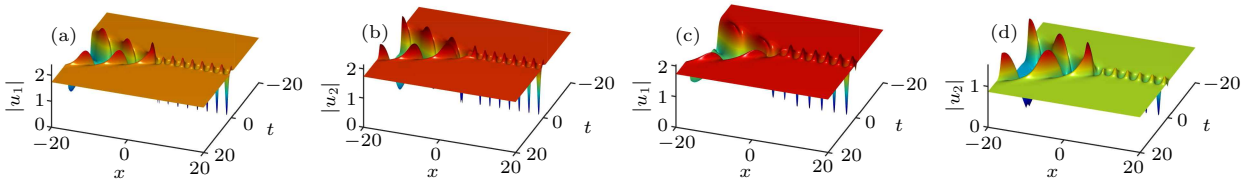


Fig. 5. The first-order breather fusion with (a), (b) $a_1=1$, $a_2=1$, $\gamma=1/10$, $\lambda_1=-\mathrm{i}\sqrt{2}/2$, $z_{10}=1$, $z_{20}=2$, $z_{30}=3$; (c), (d) $a_1=1$, $a_2=1/2$, $\gamma=1/10$, $\lambda_1=-\mathrm{i}\sqrt{2}/2$, $z_{10}=1$, $z_{20}=1$, $z_{30}=1$.

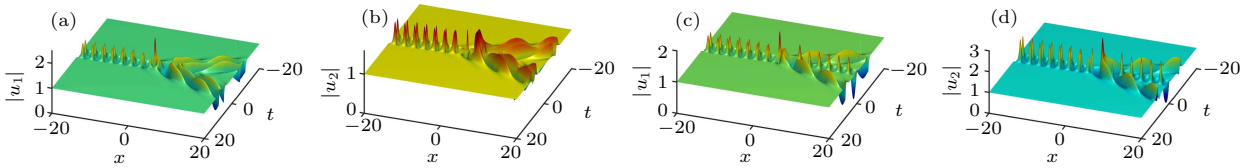


Fig. 6. The second-order breather fission with $a_1=1$, $a_2=1$, $\gamma=1/10$, $z_{10}=1$, $z_{20}=2$, $z_{30}=3$, (a), (b) $z_{11}=1$, $z_{21}=0$, $z_{31}=1$; (c), (d) $z_{11}=1000$, $z_{21}=0$, $z_{31}=1000$.

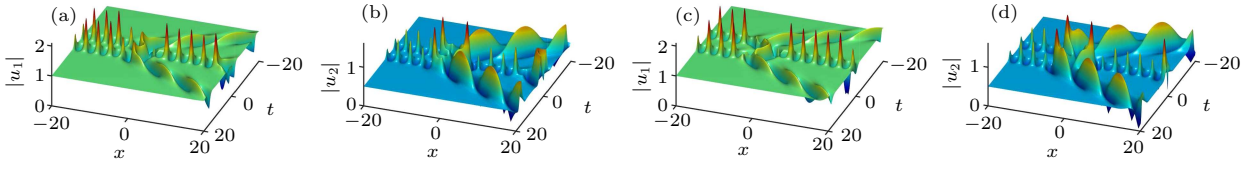


Fig. 7. The second-order breather fission with $a_1=1$, $a_2=1/2$, $\gamma=1/10$, $z_{10}=1$, $z_{20}=1$, $z_{30}=1$, (a), (b) $z_{11}=1$, $z_{21}=0$, $z_{31}=1$; (c), (d) $z_{11}=1000$, $z_{21}=0$, $z_{31}=1000$.

For $N=2$, we explore the second-order breather fission/fusion in Figs. 6 and 7. Especially, when the values of a_1, a_2 and free vectors Z_0, Z_1 change, the second-order breather fission/fusion possess distinct dynamical behaviors. Interestingly, as the values of z_{11} and z_{31} gradually increase, the distance between the two breathers gradually increases during the fission or fusion process of the breather. In addition, we also find that changing a_2 in the second-order solutions has a more obvious effect on the structures of breathers.

Case C: $\mathrm{Im}(\lambda_1) > \omega$

For $N = 1$, we take $\lambda_1 = \frac{3}{2}\mathrm{i}\omega$ which can generate the following F_0 and G_0:

$$F_0 = \begin{pmatrix} -\frac{\sqrt{5}\mathrm{i}}{5} f_0 & \frac{2\sqrt{5}\mathrm{i}}{5} a_1 \omega^{-1} \sin\left(\frac{\mathrm{i}\sqrt{5}}{2}x\right) & \frac{2\sqrt{5}\mathrm{i}}{5} a_2 \omega^{-1} \sin(\frac{\mathrm{i}\sqrt{5}}{2}x) \\ -\frac{2\sqrt{5}\mathrm{i}}{5} a_1 \omega^{-1} \sin\left(\frac{\mathrm{i}\sqrt{5}}{2}x\right) & \frac{\sqrt{5}}{5} a_1^2 \omega^{-2}(f_1 - \sqrt{5}\mathrm{e}^{\frac{3\omega}{2}x}) + \mathrm{e}^{\frac{3\omega}{2}x} & \frac{\sqrt{5}}{5} a_1 a_2 \omega^{-2}(f_1 - \sqrt{5}\mathrm{e}^{\frac{3\omega}{2}x}) \\ -\frac{2\sqrt{5}\mathrm{i}}{5} a_1 \omega^{-1} \sin\left(\frac{\mathrm{i}\sqrt{5}}{2}x\right) & \frac{\sqrt{5}}{5} a_1 a_2 \omega^{-2}(f_1 - \sqrt{5}\mathrm{e}^{\frac{3\omega}{2}x}) & \frac{\sqrt{5}}{5} a_2^2 \omega^{-2}(f_1 - \sqrt{5}\mathrm{e}^{\frac{3\omega}{2}x}) + \mathrm{e}^{\frac{3\omega}{2}x} \end{pmatrix},$$

$$G_0 = \begin{pmatrix} \frac{\sqrt{5}}{5} g_0 & \frac{2\sqrt{5}}{5} a_1 \omega^{-1} \sinh(\mu t) & \frac{2\sqrt{5}}{5} a_2 \omega^{-1} \sinh(\mu t) \\ -\frac{2\sqrt{5}}{5} a_1 \omega^{-1} \sinh(\mu t) & \frac{\sqrt{5}}{5} a_1^2 \omega^{-2}(g_1 - \sqrt{5}\mathrm{e}^{\frac{\mathrm{i}(7+75\gamma\omega^2)\omega^2}{2}t}) + \mathrm{e}^{\frac{\mathrm{i}(7+75\gamma\omega^2)\omega^2}{2}t} & \frac{\sqrt{5}}{5} \omega^{-2} a_1 a_2 (g_1 - \sqrt{5}\mathrm{e}^{\frac{\mathrm{i}(7+75\gamma\omega^2)\omega^2}{2}t}) \\ -\frac{2\sqrt{5}}{5} a_2 \omega^{-1} \sinh(\mu t) & -\frac{\sqrt{3}}{3} \omega^{-2} a_1 a_2 (g_1 - \sqrt{5}\mathrm{e}^{\frac{\mathrm{i}(7+75\gamma\omega^2)\omega^2}{2}t}) & \frac{\sqrt{5}}{5} a_2^2 \omega^{-2}(g_1 - \sqrt{5}\mathrm{e}^{\frac{\mathrm{i}(7+75\gamma\omega^2)\omega^2}{2}t}) + \mathrm{e}^{\frac{\mathrm{i}(7+75\gamma\omega^2)\omega^2}{2}t} \end{pmatrix},$$

$$f_0 = \sqrt{5}\cos\left(\frac{\mathrm{i}\sqrt{5}}{2}x\right) + 3\mathrm{i}\sin\left(\frac{\mathrm{i}\sqrt{5}}{2}x\right), \quad f_1 = \sqrt{5}\cos\left(\frac{\mathrm{i}\sqrt{5}}{2}x\right) - 3\mathrm{i}\sin\left(\frac{\mathrm{i}\sqrt{5}}{2}x\right),$$

$$g_0 = \sqrt{5}\cosh(\mu t) + 3\sinh(\mu t), \quad g_1 = -\sqrt{3}\cosh(\mu t) + \mathrm{i}\sinh(\mu t), \quad \mu = \frac{3\sqrt{5}\omega^2(1 + 11\gamma\omega^2)}{4}.$$

This case yields the breather interacting with soliton in Fig. 8. Compared with the previous two cases, we can see that the breather in Fig. 8 is quite small. It is shown that the propagation directions of the breather and soliton are coincident. For analyzing clearly the explicit collision process in this solution, the plane evolution plots are displayed in Fig. 9. It is found that if $t < 0$, the soliton is a bright soliton. However, when $t = 0$, the bright soliton decreases rapidly to zero and the breather appears. Then, when $t > 0$, the breather disappears.

For $N = 2$, we derive the second-order breather interacting with bright/dark soliton which has more complicated dynamical behaviors in Figs. 10 and 11. Notably, with the values of z_{11} and z_{31} increasing, the soliton is almost invisible. In other words, the energy to generate the soliton is small. Besides, compared with the condition of $a_1 = a_2 = 1$, the soliton under the condition of $a_1 \neq a_2$ is more obvious.

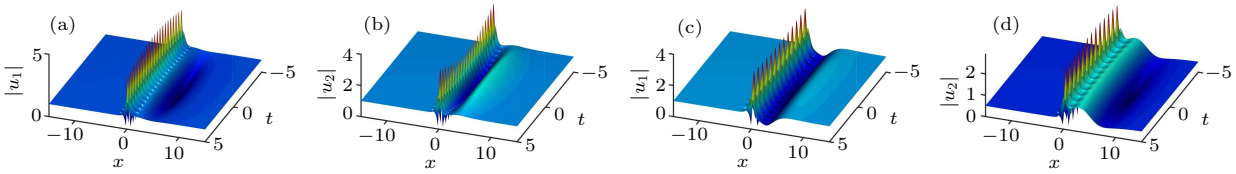


Fig. 8. The first-order breather interacts with soliton with (a), (b) $a_1 = 1$, $a_2 = 1$, $\gamma = 1/10$, $z_{10} = 1$, $z_{20} = 2$, $z_{30} = 3$; (c), (d) $a_1 = 1$, $a_2 = 1/2$, $\gamma = 1/10$, $z_{10} = 1$, $z_{20} = 1$, $z_{30} = 1$.

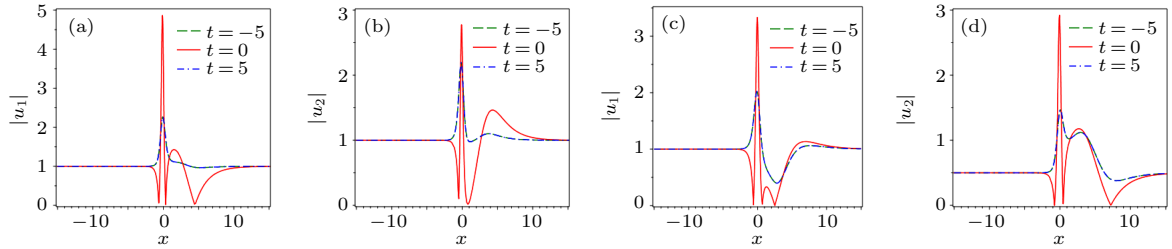


Fig. 9. The plane evolution plots of the interactional process in the breather interacting with breather with the same parameters in Fig. 8.

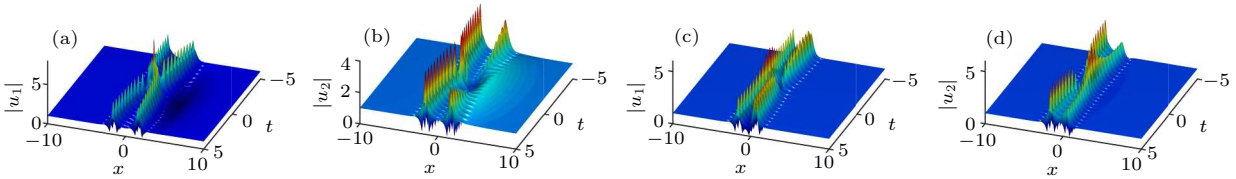


Fig. 10. The second-order breather interacts with breather with $a_1 = 1$, $a_2 = 1$, $\gamma = 1/10$, $z_{10} = 1$, $z_{20} = 2$, $z_{30} = 3$, (a), (b) $z_{11} = 1$, $z_{21} = 0$, $z_{31} = 1$; (c), (d) $z_{11} = 1000$, $z_{21} = 0$, $z_{31} = 1000$.

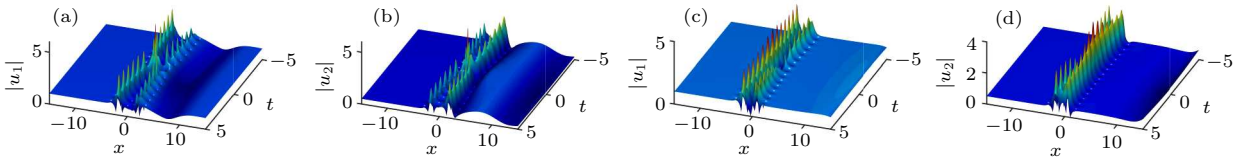


Fig. 11. The second-order breather interacts with soliton with $a_1 = 1$, $a_2 = 1/2$, $\gamma = 1/10$, $z_{10} = 1$, $z_{20} = 1$, $z_{30} = 1$, (a), (b) $z_{11} = 1$, $z_{21} = 0$, $z_{31} = 1$; (c), (d) $z_{11} = 1000$, $z_{21} = 0$, $z_{31} = 1000$.

3.2. Dynamical analysis and localized waves of 3-component Eq. (2)

Likewise, resorting to Theorems 1 and 2, one will give three kinds of localized waves of 3-component Eq. (2). The derivation process of the explicit expressions is similar to the case of 2-component and is too lengthy and hence omitted.

Case A: $\mathrm{Im}(\lambda_1) = \omega$

For $N = 1$, fixing $\lambda_1 = \mathrm{i}\omega$, we gain the first-order rogue wave interacting with breather in Fig. 12. When $a_1 = a_2 = a_3 = 1$, we notice that the breathers in u_1 and u_3 components show the bright breather, while the breather in u_2 component shows the dark breather in Figs. 12(a)–12(c). When one of a_1, a_2, a_3 is not equal to 1, Figs. 12(d)–12(f) show that the structures and amplitudes of the breathers in u_1, u_2, u_3 components are very different. That is, the values of a_1, a_2, a_3 can affect the structures, amplitudes and energy distributions of the breathers.

For $N = 2$, one can get the second-order rogue waves interacting with breathers in Fig. 13. Similarly, when $a_1 = a_2 = a_3 = 1$, two breathers in u_1 and u_3 components present two bright breathers, while two breathers in u_2 component present one bright breather and one dark breather. Furthermore, as the free vector Z_1 changes, the amplitudes of rogue waves and breathers change simultaneously. The reason for this phenomenon is that the energy of the second-order rogue waves and the energy of the breathers are converted to each other. Therefore, the total energy of this process is conversed.

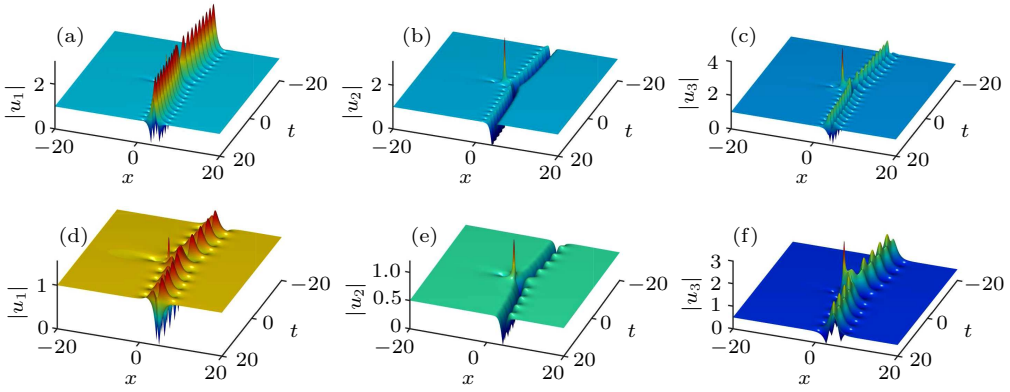


Fig. 12. The first-order rogue wave interacts with breather with (a)–(c) $a_1 = 1$, $a_2 = 1$, $a_3 = 1$, $\gamma = 1/10$, $z_{10} = 1$, $z_{20} = 2$, $z_{30} = 3$, $z_{40} = 4$; (d)–(f) $a_1 = 1$, $a_2 = 1/2$, $a_3 = 1/2$, $\gamma = 1/10$, $z_{10} = 1$, $z_{20} = 1$, $z_{30} = 1$, $z_{40} = 4$.

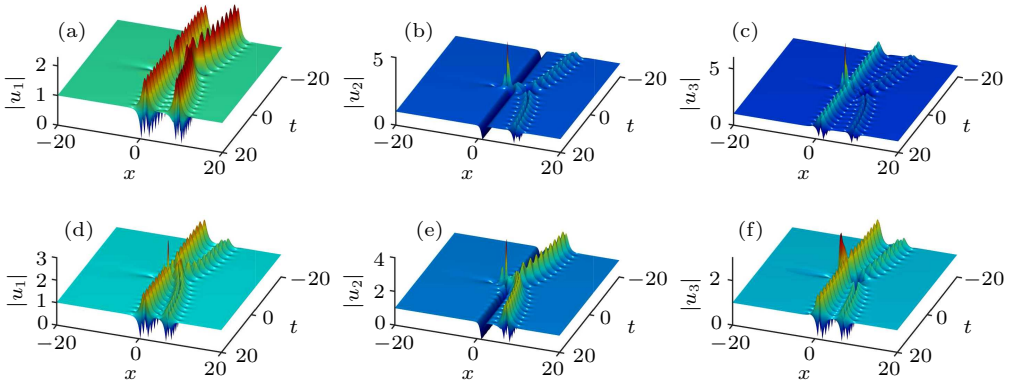


Fig. 13. The second-order rogue waves interact with breathers with $a_1 = 1$, $a_2 = 1$, $a_3 = 1$, $\gamma = 1/10$, $z_{10} = 1$, $z_{20} = 2$, $z_{30} = 3$, $z_{40} = 4$, (a)–(c) $z_{11} = 1$, $z_{21} = 0$, $z_{31} = 1$, $z_{41} = 1$; (d)–(f) $z_{11} = 1$, $z_{21} = 5$, $z_{31} = 10$, $z_{41} = 100$.

Case B: $-\omega < \mathrm{Im}(\lambda_1) < \omega$

For $N = 1$, suppose $\lambda_1 = \mathrm{i}\omega/2$, the breather fission/fusion are obtained in Fig. 14. It is obvious that breathers propagate stably at $t < 0$, while them divide at $x = 0$. At the same time, the shapes of breathers become larger and the amplitudes become smaller. It can be understood that the total energy of the

process is conserved.

For $N = 2$, we explore the second-order breather fission/fusion in Fig. 15. With the values of z_{31} and z_{41} increasing, the distance between the two breathers increase during the fission or fusion process.

Case C: $\mathrm{Im}(\lambda_1) > \omega$

For $N = 1$, setting $\lambda_1 = \frac{3}{2}\mathrm{i}\omega$ yields the breather interacting with soliton in Fig. 16. In particular, the breather is extremely different from the breather of Cases A and B. In Figs. 16(a)–16(c), we can observe that the breather in u_1 and u_2 components presents the characteristics of low amplitude in the middle and high on both sides, while the breather in u_3 component is just the opposite. This phenomenon is very readable which was never reported for multi-component equation (2). In like wise, Figs. 16(d)–16(f) are the plane evolution plots. If $t < 0$, the soliton is a bright soliton. Nevertheless, when $t = 0$, the bright soliton decreases rapidly to zero and the breather appears. When $t > 0$, the breather disappears.

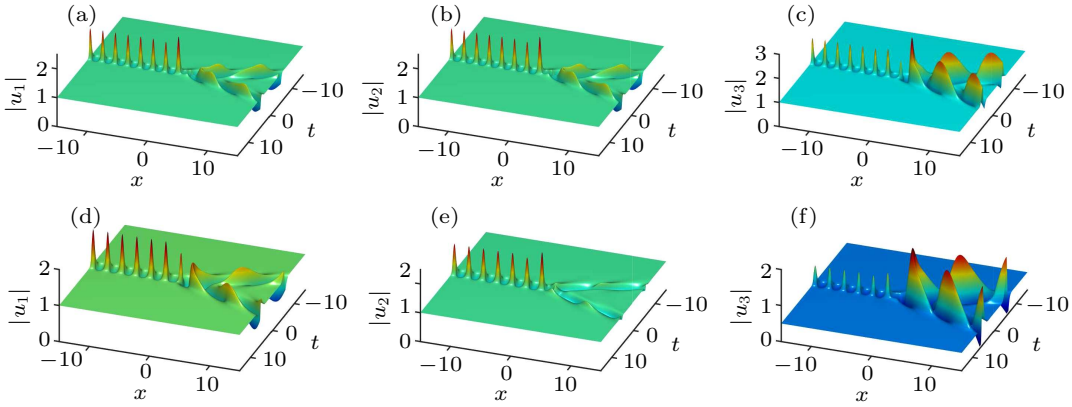


Fig. 14. The first-order breather fission with (a)–(c) $a_1 = 1$, $a_2 = 1$, $a_3 = 1$, $\gamma = 1/10$, $z_{10} = 1$, $z_{20} = 2$, $z_{30} = 10$, $z_{40} = 100$; (d)–(f) $a_1 = 1$, $a_2 = 1$, $a_3 = 1/2$, $\gamma = 1/10$, $z_{10} = 1$, $z_{20} = 2$, $z_{30} = 10$, $z_{40} = 100$.

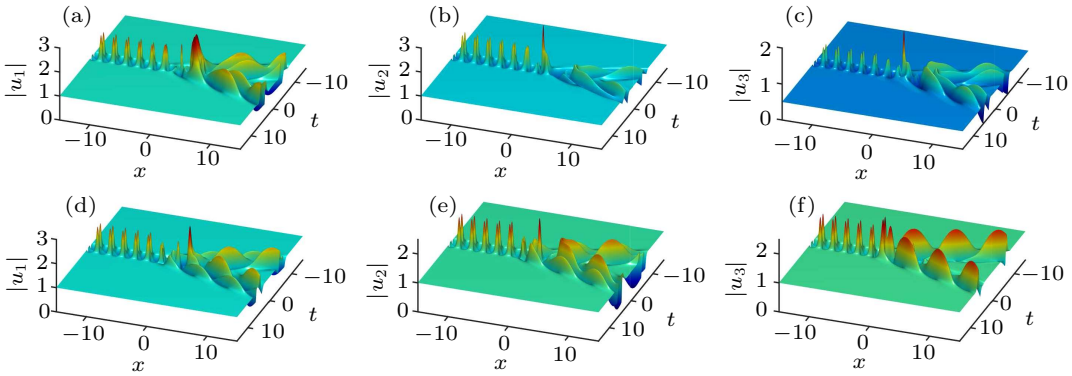


Fig. 15. The second-order breather fission with $a_1 = 1$, $a_2 = 1$, $a_3 = 1$, $\gamma = 1/10$, $z_{10} = 1$, $z_{20} = 2$, $z_{30} = 3$, $z_{40} = 4$, (a)–(c) $z_{11} = 1$, $z_{21} = 0$, $z_{31} = 1$, $z_{41} = 1$; (d)–(f) $z_{11} = 1$, $z_{21} = 5$, $z_{31} = 10$, $z_{41} = 100$.

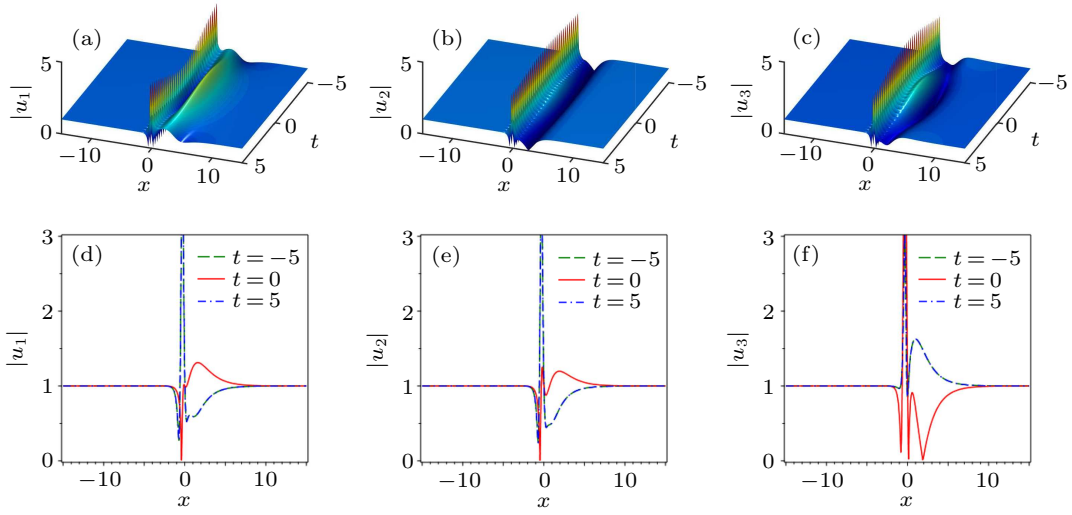


Fig. 16. The first-order breather interacts with breather with (a)–(c) $a_1 = 1$, $a_2 = 1$, $a_3 = 1$, $\gamma = 1/10$, $z_{10} = 1$, $z_{20} = 2$, $z_{30} = 3$, $z_{40} = 4$. (d)–(f) The plane evolution plots of the interactional process in the soliton interacting with breather with the same parameters.

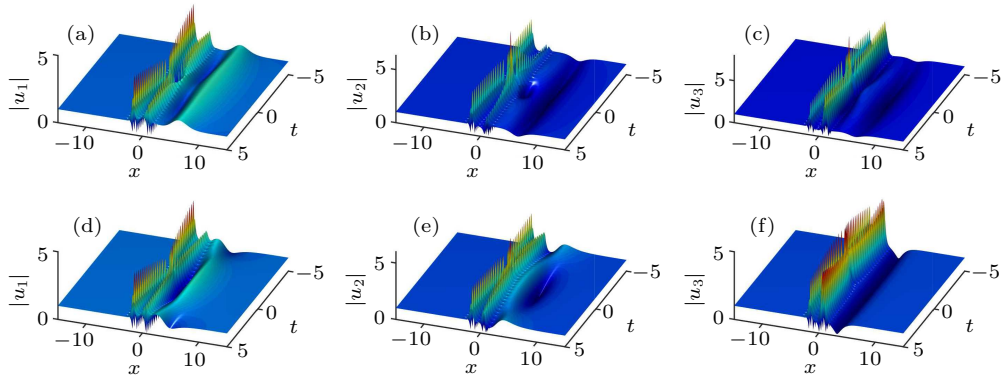


Fig. 17. The second-order breathers interact with soliton with $a_1 = 1$, $a_2 = 1$, $a_3 = 1$, $\gamma = 1/10$, $z_{10} = 1$, $z_{20} = 2$, $z_{30} = 3$, $z_{40} = 4$, (a)–(c) $z_{11} = 1$, $z_{21} = 0$, $z_{31} = 1$, $z_{41} = 1$; (d)–(f) $z_{11} = 1$, $z_{21} = 5$, $z_{31} = 10$, $z_{41} = 100$.

For $N = 2$, the second-order breathers interacting with bright/dark soliton are derived in Fig. 17. When $a_1 = a_2 = a_3 = 1$, the soliton in u_1 component exhibits the bright soliton, while the solitons in u_2 and u_3 components exhibit dark solitons. When one of a_1, a_2, a_3 is not equal to 1, the soliton in u_1 and u_2 components exhibits the bright soliton, while the soliton in u_3 component exhibits dark soliton.

4. Potential implications for fiber optics experiments and applications

4.1. Pulse manipulation and signal processing

Firstly, the discovery of various types of higher-order localized waves, such as the interaction of higher-order rogue waves with bright/antidark breathers, offers new possibilities for pulse shaping and signal processing in fiber optics. By precisely controlling the parameters that influence the formation and behavior of these waves (as demonstrated in the detailed analysis of different cases in Subsections 3.1 and 3.2), it becomes possible to engineer pulses with specific characteristics. For example, in optical communication systems, the ability to generate and manipulate rogue waves could potentially be used for high-speed data encoding. The unique waveform of rogue waves, with their peaked humps and side holes, might allow for more efficient packing of information. This could lead to an increase in the transmission capacity of fiber-optic communication links. Secondly, the breather fission and fusion phenomena observed in the study could also find applications in signal processing. For instance, in wavelength division multiplexing (WDM) systems, the controlled fission and fusion of breathers could be utilized to manage the distribution of optical power among different channels. This could help optimize the performance of the WDM system by reducing crosstalk and improving the overall signal-to-noise ratio.

4.2. Fiber device design and optimization

The solutions gained can be directly applied to the design and optimization of fiber-optic devices. For example, the understanding of how higher-order effects influence the propagation of localized waves can be used to develop more efficient fiber amplifiers. By taking into account the self-steepening and stimulated Raman scattering effects, it may be possible to design amplifiers that can better handle high-intensity ultrashort pulses without significant distortion. The study of the interaction between solitons and breathers could also inspire the design of new types of optical switches. These switches could operate based on the controlled interaction between different types of localized waves, allowing for faster and more precise switching of optical signals. This would be beneficial in applications such as optical networking and optical computing.

4.3. Nonlinear fiber characterization and measurement

The results provides a theoretical framework for more accurate characterization and measurement of nonlinear effects in fibers. By analyzing the behavior of Eq. (2) and comparing it with experimental observations of the localized waves, it becomes possible to develop more precise methods for measuring parameters such as the strength of the third-order dispersion and self-steepening. This is crucial for ensuring the quality and performance of fiber-optic communication systems. Besides, the detailed study of the energy distribution and collision processes of the localized waves can also be used to develop new diagnostic tools for fiber-optic systems. For example, by monitoring the changes in the energy distribution of the waves during propagation, it may be possible to detect and locate faults or impairments in the fiber.

4.4. Advanced fiber-optic communication systems

The advent of new types of localized waves and their associated properties may prove to be a source of inspiration for the development of more advanced fibre-optic communication systems. The capacity to generate and regulate higher-order breather fission/fusion could be employed to facilitate dynamic optical routing in optical networks. By modifying the parameters that regulate the behavior of the breather, it is possible to direct the optical signals to different destinations in accordance with the characteristics of the network traffic and

the specific requirements. Furthermore, an enhanced comprehension of the interrelationship between the various components within Eq. (2) could facilitate the advancement of more resilient and efficient space-division multiplexing (SDM) systems. By leveraging the coupling effects between disparate spatial modes or polarization states, it may be feasible to augment the number of independent data channels within a fibre, thereby enhancing the transmission capacity of the system.

5. Conclusion

At present, with the development of nonlinear optical fiber technology, the nonlinear effect of optical fibers is of great importance to restrict the bandwidth and increase the transmission distance in modern optical communication. Therefore, we focus on the n-component nonlinear Schrödinger equation with higher-order effects, which describes the ultrashort pulses in the birefringent fiber. With the aid of the Lax pair, we construct the eigenfunction and the generalized DT. By employing the generalized DT, we arrive at some novel higher-order localized waves for the 2-component and 3-component equations (2). These results can be divided into three cases: (i) $\mathrm{Im}(\lambda_1) = \omega$: higher-order rogue waves interacting with bright/antidark breathers, (ii) $-\omega < \mathrm{Im}(\lambda_1) < \omega$: higher-order breather fission/fusion, (iii) $\mathrm{Im}(\lambda_1) > \omega$: higher-order breather interacting with soliton. After that, we find that the values of a_j $(j = 1,2,\ldots,n)$ and the free vector Z in diverse cases have a great effect on the structure, collision process and energy distribution of localized waves. By means of three-dimensional figures, we discuss the dynamical behaviors of these solutions in detail. These novel results will help us understand and analyze more complicated dynamical behaviors and physical phenomena of coupled nonlinear evolution equations.

Acknowledgements

Project supported by the National Natural Science Foundation of China (Grant No. 12271096) and the Natural Science Foundation of Fujian Province (Grant No. 2021J01302).

References

[1] Ablowitz M J, Kaup D J, Newell A C and Segur H 1974 *Stud. Appl. Math.* **53** 249
[2] Mollenauer L F, Stolen R H and Gordon J P 1980 *Phys. Rev. Lett.* **45** 1095
[3] Lan Z Z, Dong S, Gao B and Shen Y J 2022 *Appl. Math. Lett.* **134** 108340
[4] Husakou A V and Herrmann J 2001 *Phys. Rev. Lett.* **87** 203901
[5] Shukla P K and Mamun A A 2003 *New J. Phys.* **5** 17
[6] Zhang G Q, Yan Z Y and Wen X Y 2018 *Phys. D* **366** 27
[7] Sun Y L, Ma W X and Yu J P 2021 *Appl. Math. Lett.* **120** 107224
[8] Li Y, Tian S F and Yang J J 2022 *Stud. Appl. Math.* **148** 1519
[9] Li Z Q, Tian S F and Yang J J 2022 *Adv. Math.* **409** 108639
[10] Li Z Q, Tian S F and Yang J J 2022 *Ann. Henri Poincar* **23** 2611
[11] Li Z Q, Tian S F, Yang J J and Fan E G 2022 *J. Differ. Equ.* **329** 31
[12] Akhmediev N N, Eleonskii V M and Kulagin N E 1985 *Zh. Eksp. Teor. Fiz.* **89** 1542
[13] Kuznetsov E A 1977 *Dokl. Akad. Nauk SSSR* **236** 575
[14] Kawata T and Inoue H 1978 *J. Phys. Soc. Jpn.* **44** 1722
[15] Ma Y C 1979 *Stud. Appl. Math.* **60** 43
[16] Dudley M, Genty G and Dias F 2009 *Opt. Express* **17** 21497
[17] Kibler B, Fatome J, Finot C, Millot G, Genty G, Wetzel B, Akhmediev N, Dias F and Dudley J M 2012 *Sci. Rep.* **2** 463
[18] Chabchoub A, Hoffmann N P and Akhmediev N 2011 *Phys. Rev. Lett.* **106** 204502
[19] Wang W, Bu L, Cheng D, Ye Y, Chen S and Baronio F 2021 *OSA Continuum* **4** 1488
[20] Solli D R, Ropers C, Koonath P and Jalali B 2007 *Nature* **450** 1054
[21] Kharif C and Pelinovsky E 2003 *Eur. J .Mech. B* **22** 603
[22] Dematteis G, Grafke T, Onorato M and Vanden-Eijnden E 2019 *Phys. Rev. X* **9** 041057
[23] Chen S S, Tian B, Tian H Y and Yang D Y 2022 *Nonlinear Dynam.* **108** 1561
[24] Tao Y S and He J S 2012 *Phys. Rev. E* **85** 026601
[25] Zhao H Q, Yuan J Y and Zhu Z N 2018 *J. Nonlinear Sci.* **28** 43
[26] Burger S, Bongs K, Dettmer S, Ertmer W and Sengstock K 1999 *Phys. Rev. Lett.* **83** 5198
[27] Baronio F, Degasperis A, Conforti M and Wabnitz S 2012 *Phys. Rev. Lett.* **109** 044102
[28] Li X L and Guo R 2022 *Commun. Nonlinear Sci. Numer. Simul.* **108** 106244
[29] Ding C C, Gao Y T, Yu X, Liu F Y and Wu X H 2022 *Nonlinear Dynam.* **109** 989
[30] Ma Y L and Li B Q 2022 *Eur. Phys. J. Plus* **137** 861
[31] Xu T and Chen G Y 2019 *Nonlinear Dynam.* **95** 87
[32] Du Z, Guo C M, Guo Q and Yuan Y Q 2022 *Phys. Scr.* **97** 075205
[33] Zhai Y Y, Hu X H, Ji T, Wei J and Li Y H 2023 *Math. Meth. Appl. Sci.* **46** 17328
[34] Ma W X 2013 *Rep. Math. Phys.* **72** 41
[35] Ma W X 2013 *Front. Math. China.* **8** 1139
[36] Rao J G, Porsezian K and He J S 2017 *Chaos* **27** 083115
[37] Peng W Q, Tian S F and Zhang T T 2019 *Math. Metho. Appl. Sci.* **42** 6865
[38] Rao J G, He J S and Cheng Y 2022 *Lett. Math. Phys.* **112** 75
[39] Guo B L, Ling L M, Liu Q P and Wu C F 2012 *Phys. Rev. E* **85** 026607
[40] Mu G and Qin Z Y 2022 *Phys. D* **435** 133287
[41] Li B Q and Ma Y L 2022 *Chaos Solitons Fract.* **156** 111832
[42] Feng B F, Ling L M and Takahashi D A 2020 *Stud. Appl. Math.* **144** 46
[43] Wei J, Geng X G and Wang X 2024 *Chin. Phys. B* **33** 070202
[44] Zhao X, Du Z, Zhou L J, Liu R X and Wang X H 2024 *Chin. Phys. B* **33** 110204
[45] He J S, Xu S W and Porsezian K 2012 *J. Phys. Soc. Jpn.* **81** 033002
[46] Bailung H, Sharma S K and Nakamura Y 2011 *Phys. Rev. Lett.* **107** 255005
[47] Setnflo L and Marklund M 2010 *J. Plasma Phys.* **76** 293
[48] Wang M, Xu T, He G L and Tian Y 2023 *Chin. Phys. B* **32** 050503
[49] Zhou Q, Zhong Y, Triki H, Sun Y Z, Xu S L, Liu W J and Biswas A 2022 *Chin. Phys. Lett.* **39** 044202
[50] Wang T Y, Zhou Q and Liu W J 2022 *Chin. Phys. B* **31** 020501
[51] Wang S B, Ma G L, Zhang X and Zhu D Y 2022 *Chin. Phys. Lett.* **39** 114202
[52] Kodama Y and Hasegawa A 1987 *IEEE J. Quantum Electron* **23** 510
[53] Mahalingam A and Porsezian K 2001 *Phys. Rev. E* **64** 046608
[54] Porsezian K and Nakkeeran K 1996 *Phys. Rev. Lett.* **76** 3955
[55] Hao R Y, Li L, Li Z H and Zhou G S 2004 *Phys. Rev. E* **70** 066603
[56] Yang G Y, Li L and Jia S T 2012 *Phys. Rev. E* **85** 046608
[57] Mirzazadeh M, Arnous A H, Mahmood M F, Zerrad E and Biswas A 2015 *Nonlinear Dynam.* **81** 277
[58] Liu D Y, Tian B and Xie X Y 2017 *Mod. Phys. Lett. B* **31** 1750067
[59] Sun W R, Li D Y and Xie X Y 2017 *Chaos* **27** 043114
[60] Xu T and He G L 2019 *Nonlinear Dynam.* **98** 1731
[61] Weng W F, Zhang G Q and Yan Z Y 2021 *Proc. R. Sco. A* **478** 20210670
[62] Zhou X M, Tian S F, Zhang L D and Zhang T T 2021 *Int. J. Comput. Math.* **98** 2504
[63] Wei H Y, Fan E G and Guo H D 2021 *Nonlinear Dynam.* **104** 649
[64] Li X L and Guo R 2023 *Ann. Phys. (Berlin)* **535** 2200472